Intraseasonal variations of water vapor in the tropical upper troposphere and tropopause region

Philip W. Mote,[1,2] Hannah L. Clark,[3] Timothy J. Dunkerton,[1] Robert S. Harwood,[3] and Hugh C. Pumphrey[3]

Abstract. We show the signature of the tropical intraseasonal oscillation (TIO) in upper tropospheric moisture and dynamical fields, roughly between 200 and 100 hPa. Relationships among these fields are examined using lag-correlation analysis and using multivariate extended empirical orthogonal functions (MEEOFs), which maximize the shared explained variance among several fields for both spatial and temporal variations. The MEEOFs show that all of the fields respond to the TIO and that the TIO is the dominant factor influencing each of the fields on these timescales. Convection associated with the TIO moistens the upper troposphere up to about 150 hPa, as expected; the behavior at 100 hPa is more complex. Over the longitude range where the TIO is associated with convection, roughly 60°–180°E, 100-hPa temperature and water vapor tend to be reduced above convection on TIO timescales. East of 180°, though, the temperature and water vapor variations at 100 hPa become decoupled. The water vapor variations, like those of 200-hPa velocity potential, appear to speed up at about 180°E.

1. Introduction

In recent years, because of its importance as a greenhouse gas, water vapor in the upper troposphere has been the focus of much interest. This interest is driven by the need to reduce uncertainty in one of the great unknowns in our understanding of Earth's climate and of the possible role of water vapor in a changing climate, and this interest is also stimulated by a recent explosion in the number and coverage of high-quality measurements of water vapor in the upper troposphere. Chief among these is the Microwave Limb Sounder (MLS) on the Upper Atmosphere Research Satellite (UARS), which has proven to be a valuable resource in filling out our knowledge of water vapor in the tropical upper troposphere [e.g., *Read et al.*, 1995; *Elson et al.*, 1996].

A curious feature of tropical climate is the appearance of coherent, eastward moving variations in winds and convection with a timescale of 30–60 days; this feature is known as the Madden-Julian oscillation or the tropical intraseasonal oscillation (TIO) and has been documented in numerous meteorological studies (see the review article of *Madden and Julian* [1994]). Since *Madden and Julian* [1972] pointed out the signature of the TIO on 100-hPa temperature, less attention has been paid to the upper troposphere and tropopause region than to the lower troposphere. Deep convection, which reaches the upper troposphere, is often identified using outgoing longwave radiation (OLR) and has been used in several studies of the TIO [e.g., *Kiladis and Weickmann*, 1992; *Wheeler and Kiladis*, 1999]. *Brown and Zhang* [1997] showed that high-level cloudiness and humidity throughout the troposphere had fundamentally different characteristics during the moist and dry phases of the TIO. Recently, *Clark et al.* [1998] examined longitude-time sections of MLS water vapor in the upper troposphere at tropical latitudes and identified eastward moving moist and dry features that varied on intraseasonal timescales. Spectral characteristics obtained from wavenumber-frequency diagrams and from analysis using extended empirical orthogonal functions (EEOFs) revealed a zonally symmetric component at 70 days and an eastward traveling component at 30–60 days. The spectral characteristics in time and space were consistent with those expected for the TIO. Enhanced water vapor coincided with strong 850-hPa westerly wind bursts from the Indian Ocean to the western Pacific, which are known to play an important role in TIO events and possibly also in the initiation of El Niño events [e.g., *McPhaden*, 1999].

Clark et al. [1998] focused on one particular moist phase of the TIO in early 1992 and examined sequences of 5-day averaged fields of water vapor and vertical ve- ty. The water vapor 'life cycle' was characteristic

[1] Northwest Research Associates, Bellevue, Washington

[2] Also at Climate Impacts Group, Joint Institute for the Study of the Atmosphere and Oceans, University of Washington, Seattle.

[3] Department of Meteorology, University of Edinburgh, UK

of TIO events and compared well with the life cycle in OLR described in many studies. However, *Clark et al.* [1998] did not quantify the connections between water vapor and other fields, nor did they show how water vapor was linked to OLR or other measures of the TIO.

This paper explores and quantifies the relationships among upper tropospheric water vapor, meteorological fields, and OLR, the last of which provides a good indication of convective activity. We also investigate the extent to which the TIO may affect conditions at 100 hPa near the tropical tropopause, where *Mote et al.* [1998] noted a 30- to 60-day spectral peak in water vapor measured by MLS. We look at both the life cycle and the space-time variations of the TIO, objectively linking the variations among several fields using multivariate extended empirical orthogonal functions (MEEOFs), which are explained in section 4. MEEOFs, which were previously used by *Dunkerton and Baldwin* [1995], offer an efficient way to study coherent variations among several fields, whereas other methods (e.g., coherence or singular value decomposition) are useful for linking variations between only two fields.

2. Data

The meteorological data used in our analyses come from the European Centre for Medium-Range Weather Forecasts (ECMWF) Reanalyses (ERA) [*Gibson et al.*, 1997]. Data are available at $2.5° \times 2.5°$ horizontal resolution on several standard pressure surfaces. Fields used here are 100-hPa temperature and 200-hPa velocity potential, which is derived from the wind field.

Upper tropospheric water vapor data come from the Microwave Limb Sounder (MLS), an instrument on the Upper Atmosphere Research Satellite (UARS). The UARS is in a polar orbit with an inclination of $57°$ to the equator [*Reber*, 1993], making 15 orbits each day, with adjacent orbits being separated by about 2670 km at the equator. The satellite performs a yaw maneuver about every 36 days, but the tropical region is observed daily, enabling a nearly continuous time series to be constructed. The MLS instrument is described in more detail by *Barath et al.* [1993], and the measurement technique is described by *Waters* [1993].

Two MLS radiometers are used for measuring water vapor, corresponding to spectral bands at 205 and 183 GHz. The 205-GHz radiometer is sensitive to water vapor in the upper troposphere when concentrations are in the range of 100–300 ppmv [*Read et al.*, 1995]. The best sensitivity occurs when the water vapor concentration is about 150 ppmv; of the standard UARS pressure levels, it is at 215 hPa ($\sim$12 km at low latitudes) that this concentration most often occurs. For consistency with *Clark et al.* [1998], who used Version 422 data, and (more important) because V422 remains the only version for which a validation paper has been published [*Read et al.*, 1995], we use V422 in this paper as well. Newer versions (V490 and V5) of MLS data are

now available, and V490 is of higher quality than either V422 or V5 (W. Read, personal communication, 2000), but the variations in V422 and V490 are very similar (correlation 0.95 for daily variations in the $0°-10°$S latitude band). We also examined variations at 147 hPa, the highest level for which MLS upper tropospheric data are retrieved, and found the V422 data again very similar to V490 (correlation 0.94). One drawback with using V490 and V5 for intraseasonal studies is that the UARS yaw cycle, whose period (average about 36 days) falls within the range of periods of interest here, is more apparent in these later versions.

The other MLS radiometer that retrieves water vapor uses the 183-GHz band, which is most sensitive to water vapor in the stratosphere and mesosphere. A nonlinear retrieval, described by *Pumphrey* [1999], offers many advantages over the standard linear retrieval and has been used in a few previous studies [e.g., *Mote et al.*, 1996, 1998]. It extends the range of the retrieval down to 100 hPa with a higher vertical resolution than the standard retrieval; the next highest level is at 68 hPa. In this paper we use the 100-hPa data from the nonlinear retrieval (V0104), which exhibit variations on intraseasonal timescales [*Mote et al.*, 1998].

The 100-hPa data have some shortcomings that must be discussed. First, the retrieval reports that the data are often strongly influenced by the a priori profiles, so that the reported variations are probably smaller than the observed spatial variations. Despite the weakness of the signal, the variations that are derived are broadly consistent with both expected seasonal variations in water vapor [*Mote et al.*, 1996] and higher-frequency variations [*Mote et al.*, 1998]. The reliance on monthly-mean, zonal-mean climatology, however, means that the retrieved water vapor values jump abruptly from the end of one calendar month to the beginning of the next. It is straightforward to remove this effect by subtracting the zonal mean, as was done in the previous studies.

Second, the vertical resolution at 100 hPa is nearly 4 km, so one might assume that the retrieval of 100-hPa water vapor in the tropics feels some influence from upper tropospheric water vapor. In fact, the upper tropospheric water vapor probably has little influence on the retrieved 100-hPa data, for two reasons. (1) The retrieval code ignores radiances with a tangent pressure below about 100 hPa, with the result that the averaging kernel for 100 hPa actually peaks near 68 hPa [*Pumphrey*, 1999], and (2) the retrieval has to fit radiances from several closely spaced tangent heights between 100 and 46 hPa. While the bottom one or two may contain radiance from the upper troposphere, the next two or three will contain less of this. The retrieval has to fit them all, which it can do best by choosing a profile that is not influenced much by the upper troposphere. In short, the 100 hPa water vapor product is influenced primarily by water vapor in a layer in the lower stratosphere and not much by water vapor in the upper troposphere.

Outgoing longwave radiation (OLR) data come from National Oceanic and Atmospheric Administration polar orbiting satellites and have been subjected to quality control and then interpolated in time and space as described by *Liebmann and Smith* [1996]. The interpolated data are available as daily averages on a 2.5° × 2.5° latitude-longitude grid and have no missing values.

Daily ERA and OLR data are available over a period of record spanning decades, but for this study we confine attention to a period of 19 months (which include two northern winters) when the 183-GHz radiometer was operating: October 1, 1991, to April 30, 1993. This time period, which includes the Tropical Ocean-Global Atmosphere/Coupled Ocean-Atmosphere Response Experiment (TOGA/COARE) Intensive Observing Period, is fairly representative of the climatological TIO behavior [*Chen and Yanai*, 2000]. For the time-longitude sections used in the EEOF and MEEOF analysis, we average data between 10°S and the equator, taking advantage of the large spatial scale of the TIO and the coherence of features across this latitude range on this timescale. MLS profiles between 10°S and the equator are binned in 24° longitude bins, consistent with the large-scale nature of the TIO.

3. Spatial Relationships Among Fields

3.1. Outgoing Longwave Radiation

Clark et al. [1998] studied a sequence of 5-day averaged maps of water vapor, taken during a TIO event between December 1991 and February 1992. The sequence corresponded to one of the eastward moving moist events seen in the longitude-time section at 10°S (their Plate 1d). The water vapor field was compared with vertical velocity from ECMWF reanalysis to identify regions of convection. Strong upward motion in the middle troposphere coincided with enhanced water vapor in the upper troposphere.

Here we compare water vapor with outgoing longwave radiation for the same sequence of days. Figure 1 shows mixing ratios of water vapor at 215 hPa which are greater than 170 ppmv, and OLR emitting at less than 225 W m^{-2}, the same threshold value used by *Matthews et al.* [1996] to indicate enhanced convection during the TIO event of March 1988. It is clear from this figure that the water vapor and OLR fields are similar, and that convection moistens the upper troposphere within a fairly large area around the convection. It is also clear that some of these features propagate eastward, for example, the convective activity north of Australia on January 1 that travels east of the date line and then dies out by February 15. Note also that the features span a wide range of latitudes but are generally centered south of the equator.

3.2. Velocity Potential and Water Vapor

In general, at most tropical locations, water vapor and 200-hPa velocity potential are anticorrelated (not shown). That is, large-scale divergence (generally indicated by negative velocity potential) is locally associated with enhanced water vapor, and convergence is locally associated with reduced water vapor. Since large-scale upper level divergence is broadly associated with convection, this negative correlation reflects the well-known fact that convection tends to moisten the upper troposphere (as was emphasized in Figure 1).

Many studies [e.g., *Hendon and Salby*, 1994; *Knutson and Weickmann*, 1987; *Matthews and Kiladis*, 1999] have investigated the life cycle of the TIO through spatial regression maps of dynamical fields and OLR. In a similar manner, we use a reference time series of 200-hPa ECMWF velocity potential at 11.25°S and 168.75°E, the point at which it has maximum variance, to calculate one-point correlation maps of water vapor at various lags (Plate 1). The correlations are calculated using data from December 1, 1991, until March 31, 1992, a period when the TIO was strong. A positive time lag means the water vapor field lags the velocity potential field, and a negative time lag means the water vapor field leads the velocity potential field.

In contrast to Figure 1, evidence of eastward propagation in Plate 1 is more subtle. A dry feature (negative correlation) can be seen moving eastward through the reference point from about day -15 to day +15. The plate reveals two noteworthy aspects of the water vapor response to the TIO: first, the spatial pattern, and second, a strong projection onto a 50-day timescale. The spatial pattern associated with maximum velocity potential (lag 0) at the reference point (corresponding to maximum convergence and minimum convection) consists of a large area of reduced water vapor surrounding the reference point and extending into the Northern Hemisphere. Ringing this is an arc of enhanced water vapor extending from the Bay of Bengal to Hawaii. At lags of ±25 days the pattern is almost the same as at lag 0, only in reverse, strongly pointing to a 50-day timescale. These features suggest that the TIO influences the circulation and moisture distribution of the upper troposphere over a wide area and that the response is largely through a Hadley-Walker type circulation with subtropical subsidence in the Northern Hemisphere ringing tropical convection at, and just south of, the equator.

4. EEOF and MEEOF Analysis Procedure

In the previous section we used maps and correlations to demonstrate the relationships between two fields. However, considering more than two fields becomes extremely difficult, and the spatial detail in the maps can obscure the basic relationships. In order to simplify the TIO-related fluctuations in the fields under consideration here (water vapor at two levels, temperature, OLR, and velocity potential), we describe a technique called MEEOF analysis, an extension of the commonly used empirical orthogonal function (EOF) analysis. EOF
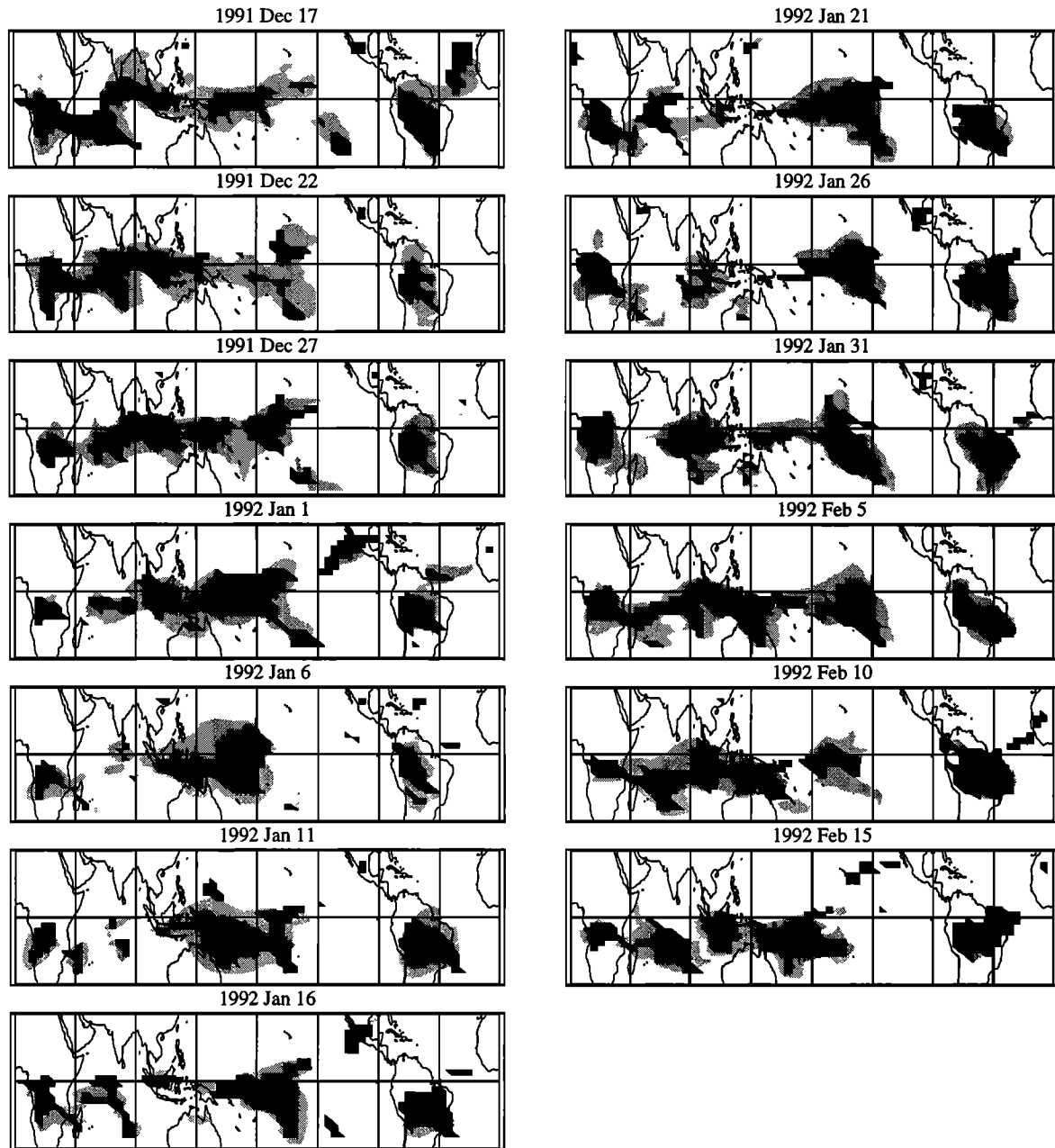
Figure 1. Five-day averages of water vapor mixing ratios at 215 hPa greater than 170 ppmv (shaded regions) and of outgoing longwave radiation (OLR) less than 225 W m^{-2} (solid regions). Dates indicate the middle of the pentad.

analysis is useful for finding coherent spatial patterns in noisy data. In this section we explain extended EOFs (EEOFs), which are useful for identifying coherent patterns of spatiotemporal variations, and MEEOFs (multivariate EEOFs), which are useful for identifying coherent spatiotemporal variations among several fields.

EEOFs [e.g., *Weare and Nasstrom*, 1982; *Clark et al.*, 1998] for longitude-time sections $x(\lambda, t)$ are calculated by first forming a vector at each time t made up of the time series x at each of L longitudes and each of $2N+1$ lag times:

$$x(\lambda = 1, t - N\Delta t), x(\lambda = 1, t - (N-1)\Delta t), ...,$$
$$x(\lambda = 1, t), ...x(\lambda = 1, t + N\Delta t),$$
$$x(\lambda = 2, t - N\Delta t), ...,$$
$$x(\lambda = L, t + N\Delta t).$$

The covariances are then calculated, leading to a square covariance matrix with dimension $L(2N+1)$. EOFs are then calculated in the usual manner, leading to patterns (EEOFs) that maximize the explained spatiotemporal variance. The EEOFs calculated here are fairly insen-
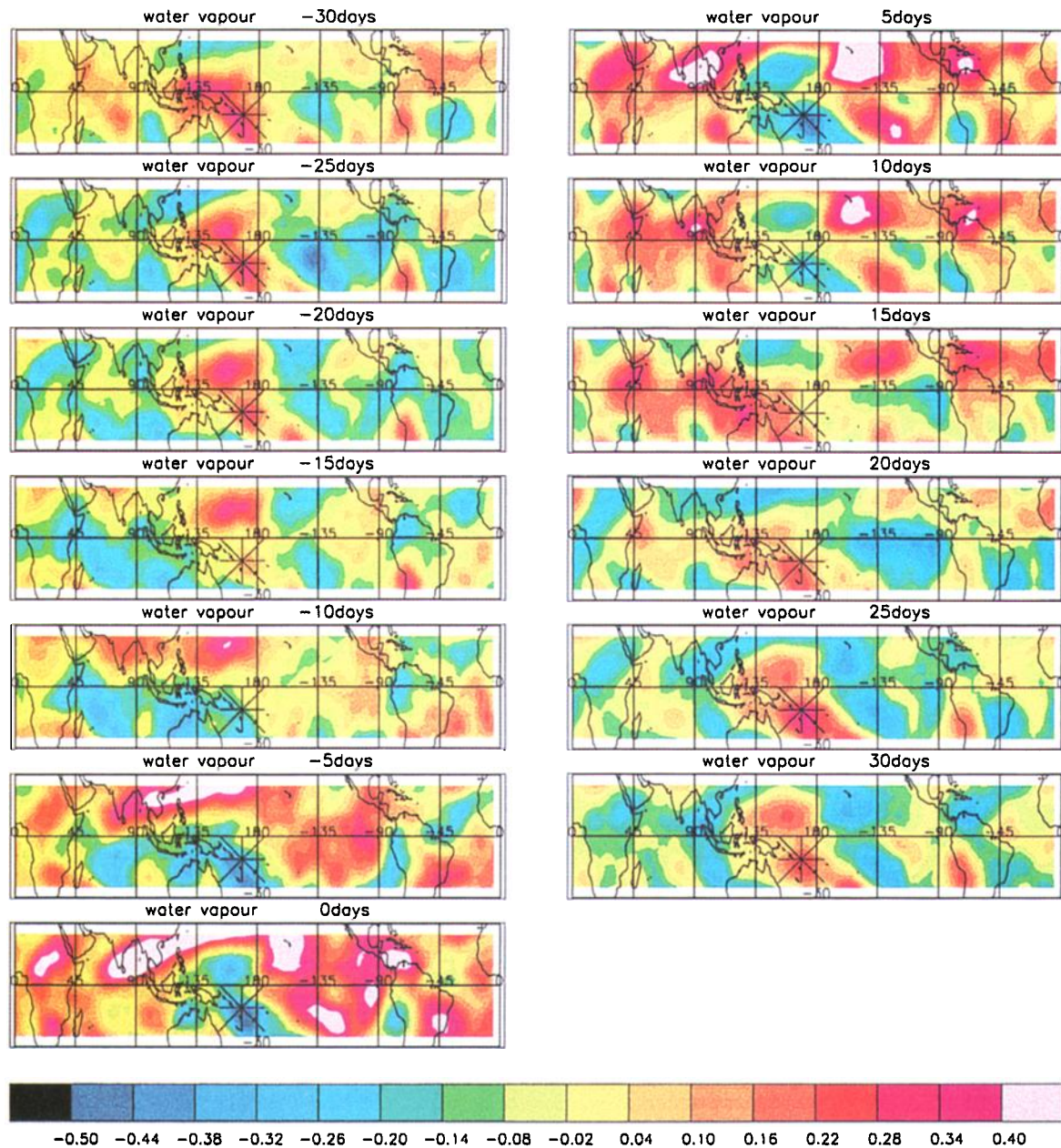
Plate 1. One-point correlation maps at various lead and lag times, showing the correlation between Microwave Limb Sounder (MLS) water vapor at 215-hPa and a reference time series of 200-hPa European Centre for Medium-Range Weather Forecasts (ECMWF) velocity potential at 11.25°S, 168.75°E, indicated by the large asterisks.

sitive to the choice of lag interval (the results here used an interval of 5 days) and to longer windows (30 days here). We present the results of the EEOF analysis in section 5.

The MEEOF calculation is performed by concatenating the vectors for each of the F variables, so that at time t the vector would be as above but for each variable:

$$\chi_{200}(\lambda = 1, t - N\Delta t), ..., \chi_{200}(\lambda = L, t + N\Delta t),$$

$$\text{OLR}(\lambda = 1, t - N\Delta t), ..., \text{OLR}(\lambda = L, t + N\Delta t),$$

$$Q_{215}(\lambda = 1, t - N\Delta t), ..., Q_{215}(\lambda = L, t + N\Delta t),$$

$$T_{100}(\lambda = 1, t - N\Delta t), ..., T_{100}(\lambda = L, t + N\Delta t),$$

$$Q_{100}(\lambda = 1, t - N\Delta t), ..., Q_{100}(\lambda = L, t + N\Delta t).$$

The order of the variables is immaterial, but they must be normalized so that the MEEOFs reflect physical variations and not the unit used to measure the variables. Once the MEEOFs are calculated, they can be separated into the corresponding component for each variable, here called EEOF_m; the EEOF_m then illustrate each field's response to coherent variations across all the fields.

For the detailed analysis in sections 5 and 6, we go through several steps in processing the data. Longitude-time slices are formed using averages between the equator and 10°S. Then, in order to focus on the timescale of interest (5–90 days), we band-pass filter each of the data sets. The data sets with higher horizontal resolution (ERA and OLR) are interpolated to the 24° longitudinal resolution at which the 100-hPa water vapor data have been binned. Finally, the fields are normalized using the mean and standard deviation of the resulting longitude-time slice. The MEEOF calculation involves inverting a square covariance matrix whose dimension varies as the square of the product of the number of fields, the number of longitudes, and the number of time lags. The relatively low spatial resolution used here represents a balance between computational efficiency and spatial detail but is adequate to resolve the main patterns of interest.

5. Response of Each Field to the TIO

The procedure described in section 4 was applied to the longitude-time sections of data averaged over 0°–10°S for each of the five variables and also to longitude-time sections at the equator and 10°S (though we only show results for the 0°–10°S averages). *Clark et al.* [1998] showed the EEOFs for water vapor at 215 hPa, 10°S, along with a comparison of Hovmöller (longitude-time) diagrams from the MLS data and from reconstructions using the first few EEOFs. Here we show (1) representative EEOFs from 200 hPa velocity potential, (2) Hovmöller diagrams for the upper tropospheric data, and (3) Hovmöller diagrams reconstructed from the leading EEOFs.
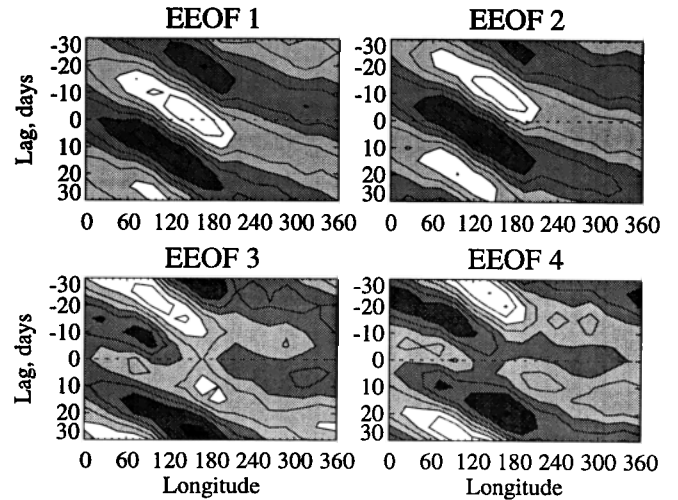

Figure 2. Extended empirical orthogonal functions (EEOFs) for 200-hPa velocity potential averaged over 0°–10°S.

Figure 2 shows the first four EEOFs for the 200 hPa velocity potential. All four are dominated by eastward moving features, with maximum variance between 60° and 180° east longitude, and the four represent two conjugate pairs. (Conjugate pairs of EOFs are typical for propagating features; their spatial structures are similar but 90° out of phase, and their principal component time series are also typically a quarter cycle out of phase. For an example, see *Mote et al.* [1998].) Furthermore, all four show a distinct difference in phase speed in the Eastern and Western Hemispheres. The phase speed for the first two EEOFs in the Eastern Hemisphere is about 8 m s^{-1}, while in the western Hemisphere it is about 15 m s^{-1}. Previous work [*Hendon and Salby*, 1994; *Hendon and Glick*, 1997] has suggested that the slower propagating feature is governed by moist dynamics over the Indian and Western Pacific Oceans and that the faster moving feature is governed by dry dynamics over the rest of the tropics.

The characteristic period of the features identified by these EEOFs is about 40 days for the first pair of EEOFs. For the second pair the structures are more complex, and it is difficult to ascribe a period to the features, but spectral analysis of the principal component time series (not shown) reveals peaks at 56 and 31 days, and little power between 34 and 46 days, for the second pair of EEOFs. The time series of all four EEOFs also reveal that the dominant activity occurs during Southern Hemisphere summer; the amplitudes of all four EEOFs diminish considerably during southern winter.

The eigenvalues of the EEOFs of all five fields (Figure 3) share certain characteristics. The first pair are nearly equal, as is usual for eigenmodes that come in conjugate pairs. After a certain eigenmode (the fourth for velocity potential and OLR and the second for the two water vapor fields and 100-hPa temperature), there is little separation between successive eigenvalues. Be-
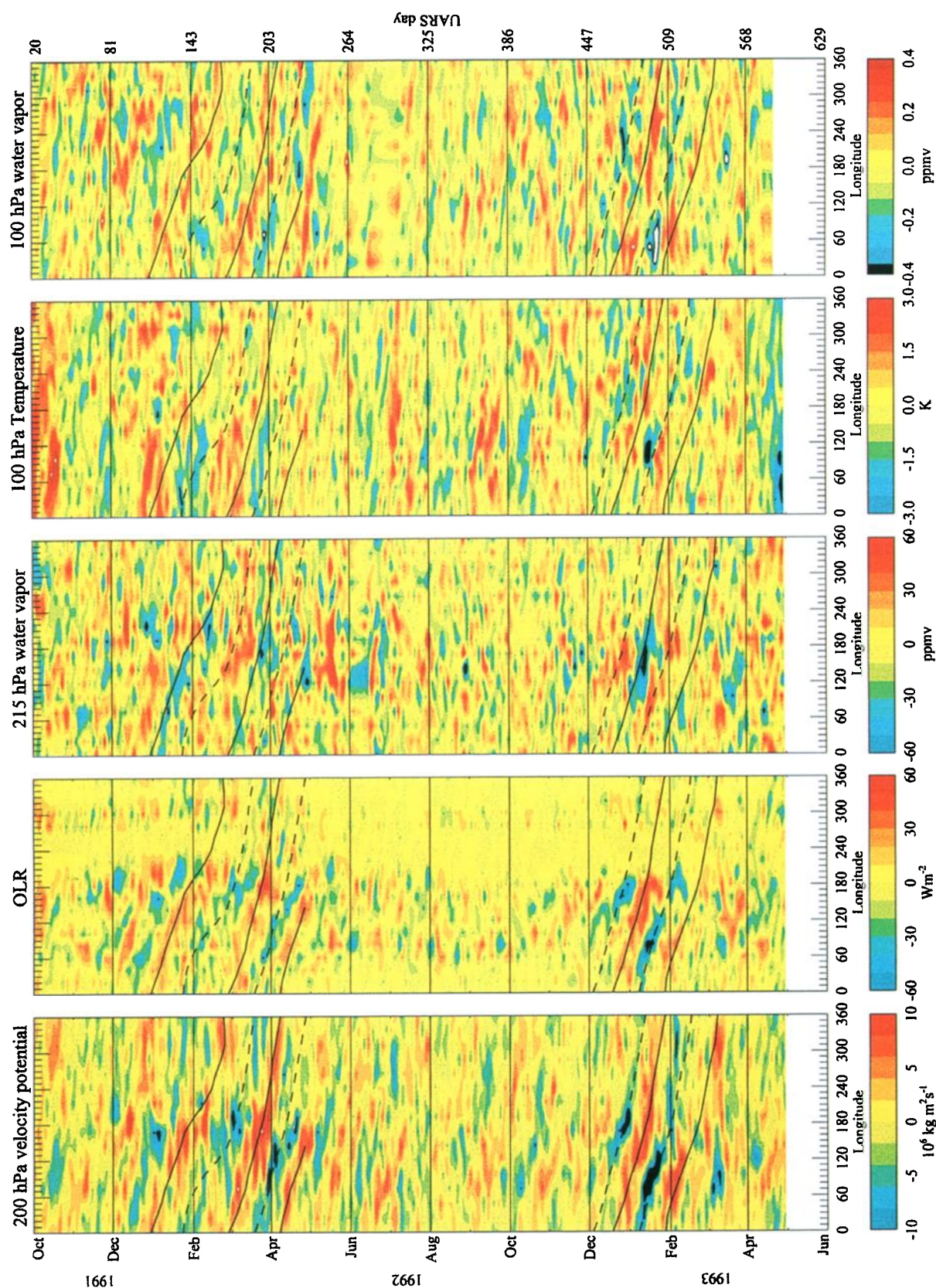
Plate 2. Hovmöller plots for the indicated fields. The color convention is such that low values are blue and high values are red. The range of values is about 160 W m^{-2} for OLR and about 180 ppmv for water vapor. The bold curves trace features in the velocity potential (see Plate 3 caption).
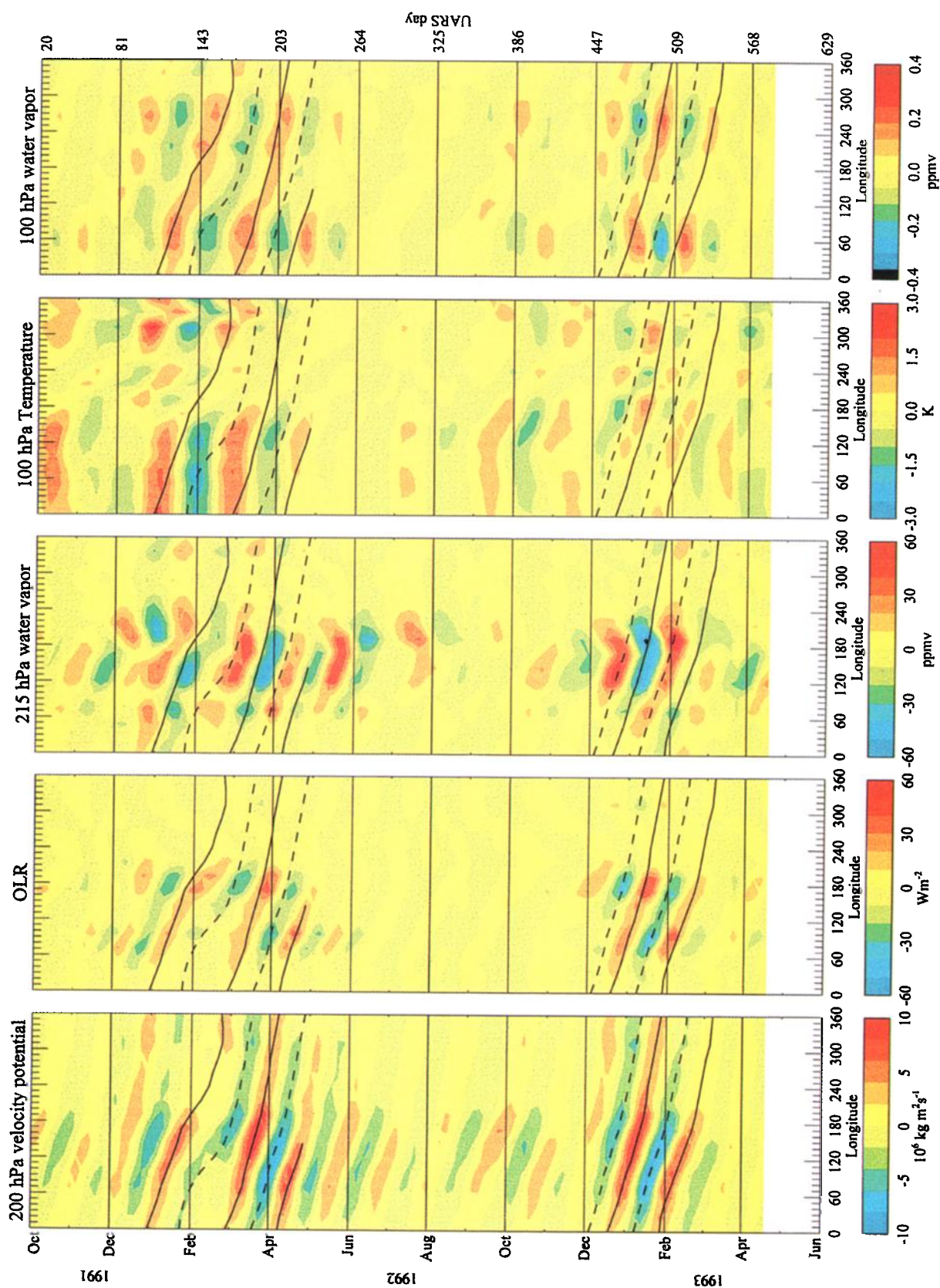
Plate 3. Hovmöller plots for the fields in Plate 2, reconstructed from the first four EEOFs of each field. The bold curves here and in Plate 2 were formed by tracing features in the left-hand panel here.
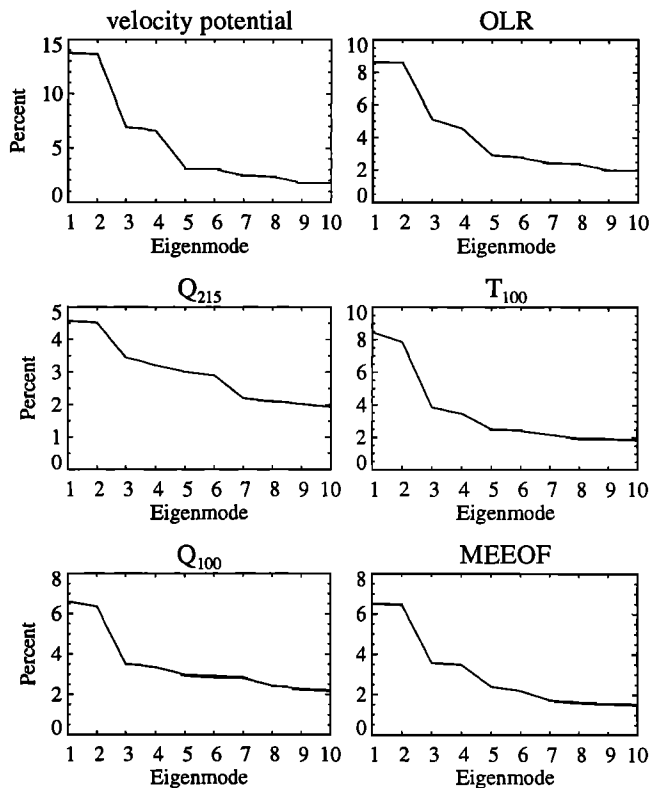
Figure 3. Percentage variance explained by the first 10 eigenmodes of the EEOF analysis and (lower right hand corner) the multivariate EEOF (MEEOF) analysis.

cause separation is an indication of significance, we may safely ignore modes higher than 4; indeed, their structure is often difficult to interpret physically.

While the percentage variance explained by each mode seems relatively small compared with that for spatial EOFs, this is a characteristic of EEOFs, because the temporal variations introduce considerable complications for statistical modes to explain. The low percentages also occur in part because of the time filtering used: The band-pass filter included periods as short as 5 days, which was also the interval used for the EEOF analysis. When the band-pass filter was modified to pass only periods greater than 20 days, the EEOFs were essentially the same, but the percentage variance explained by the leading modes increased by about 50% for each of the five fields.

In Plate 2 we show Hovmöller plots of the original band-pass-filtered data. Velocity potential is inherently a large-scale field, emphasizing the gravest modes of the global divergence field; OLR is inherently a small-scale field. Nonetheless, there is a clear correspondence between the two fields as highlighted by the feature-tracking curves, and the two fields tend to be positively correlated. That is, areas of divergence at 200 hPa (blue) are associated with anomalously low values of OLR (also blue); since the high cloud tops characteristic of low OLR are also associated with deep convection, these two fields taken together indicate their similarity

on these timescales despite their fundamentally different spatial scales. For upper tropospheric water vapor, similar eastward moving features are seen, as shown by *Clark et al.* [1998], but with opposite sign: Low OLR (convection) is associated with high values of water vapor, as was plain in Figure 1.

These relationships are plainer when the fields are reconstructed with the leading EEOFs. EEOFs like those shown in Figure 2 were calculated for the other four fields as well. Using the first four EEOFs, we have reconstructed Hovmöller plots and show them in Plate 3. This plate highlights the coherent, eastward propagating features shown in Plate 2 and emphasizes the correspondence among the fields, even though the EEOFs were derived independently. It also emphasizes the continuation of eastward propagating features in the velocity potential during southern winter, even though there is little indication of such features in the other two upper tropospheric fields. Evidently, the dry eastward modes in the eastern Pacific can exist even when the convective part of the TIO is inactive.

The relation of 215- and 100- hPa water vapor is such that anomalies are out of phase between the two levels during intraseasonal oscillation events. For each of the phase lines displayed in the middle and right-most panels of Plate 2, the prevailing tendency is for anomalies at 100 hPa to be opposite in sign to those at 215 hPa. This is seen in both Southern Hemisphere summers, although in the second summer (1992–1993), the 100-hPa water vapor signal extends farther into the Western Hemisphere. As with velocity potential, the water vapor anomaly is visible at all longitudes. In this respect, the behavior of water vapor, particularly at 100 hPa, differs from that of OLR and 100-hPa temperature, for which intraseasonal variability is confined primarily to the Eastern Hemisphere and the region of the date line.

At 100 hPa the intraseasonal variations in both temperature and water vapor have a rather different character from the variations in upper tropospheric fields. Variance is more zonally distributed, whereas for the upper tropospheric fields it is more zonally confined between roughly 90° and 210° (though these limits are somewhat different for the different fields). For water vapor, some of the eastward propagating features correspond well with those of 200-hPa velocity potential, as indicated by the curves that are overplotted. (This is more apparent when the fields are reconstructed using EEOFs; see Plate 3.) The correspondence is weaker for temperature.

6. Relationships Among Fields: The Utility of MEEOFs

The MEEOF technique described in section 4 provides a useful way to relate the variations of the five fields. Once the MEEOFs have been calculated, the contribution from each field can be extracted and the corresponding EEOFs shown (Figure 4). That is, the
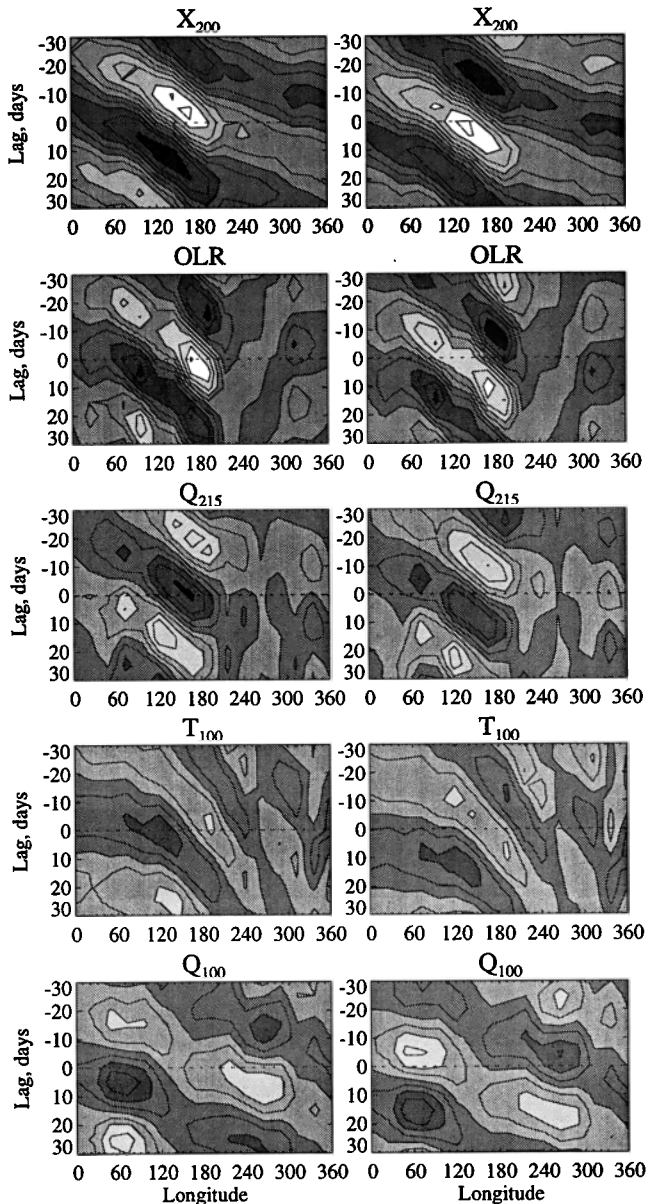
Figure 4. Structure of the two leading $EEOF_m$ for each of the five fields, derived for all five fields simultaneously. Left column shows first MEEOF; right column shows second MEEOF.

fields were all derived together, and together the EEOFs explain the largest fraction of the combined variance, but are shown separately. These EEOFs are distinct from the EEOFs discussed earlier, which were derived for each field independently; like the earlier EEOFs, the two shown here form a conjugate pair. For clarity in the subsequent discussion we refer to the EEOFs calculated independently as $EEOF_i$ and we refer to the EEOFs extracted from the MEEOFs as $EEOF_m$.

The first two $EEOF_m$ for all five variables show evidence of eastward propagation, and the tropospheric fields (top three) and 100 hPa temperature also show

evidence of a change in characteristics of propagation at around 210° longitude: Variations become much weaker, even incoherent. In the case of velocity potential, the variations east of 210° also have higher phase speed, as noted earlier. By contrast, the 100-hPa temperature variations seem to have smaller phase speed in the Western Hemisphere; examination of longitude-height cross sections reveals that the change in zonal phase speed is probably related to a change in vertical phase speed (G. Kiladis, personal communication, 2000). A change in phase tilt could explain these changes. For water vapor at 100 hPa, the $EEOF_m$ also show some eastward propagation, though the pattern is somewhat less coherent.

For all variables the first two $EEOF_m$ clearly represent a conjugate pair. That is, they have similar wavy spatial structure and are about a quarter of a cycle apart. Therefore each of the fields is strongly affected by a propagating disturbance; its characteristic timescale is of the order of 40–50 days. The fact that the phases line up so well indicates common causality.

6.1. Relationship Between MEEOFs and EEOFs

By construction, MEEOFs maximize the combined variance of all the fields. Is it possible, however, that the MEEOFs are artificially selecting variations that are not the dominant variations for one or more of the fields? We can check for such artificial selection by comparing the $EEOF_m$ with the $EEOF_i$, in particular calculating the correlation in the longitude-lag space of EEOFs. If they are very similar, then the variation identified by the MEEOFs is the dominant variation. For velocity potential, the leading pair of $EEOF_m$ looks very similar to the leading pair of $EEOF_i$ (Figure 2), except that the phasing is somewhat different. Lag correlations of the principal component time series reveal that the first $EEOF_m$ is 5 days ahead of the first $EEOF_i$, with a correlation between the two time series of 0.94.

Table 1 shows, for each field, the correlations between the $EEOF_i$ and the $EEOF_m$. The phase shift of the first two $EEOF_m$ for velocity potential reduces the correlations, but they are fundamentally the same as the $EEOF_i$. For OLR and 215-hPa water vapor, the first two $EEOF_m$ are nearly the same as the $EEOF_i$, as indicated by the fairly high (above 0.9) absolute correlations. The variations identified by the MEEOF approach are indeed the dominant story for those fields. The third and fourth $EEOF_m$ are quite similar to the third and fourth $EEOF_i$ only for velocity potential. For 100-hPa temperature, the weak correlations between the first two $EEOF_m$ and the first two $EEOF_i$ are only partly because of phase shifting. Despite the weak relationship between the $EEOF_m$ and $EEOF_i$ for temperature, water vapor at 100 hPa has a fairly strong similarity between the $EEOF_m$ and the $EEOF_i$, indicating that it is better connected to the tropospheric fields (as was apparent in Plate 3).

Table 1. Correlations Between $EEOF_m$ and $EEOF_l$

EEOF	EEOF Number			
	1	2	3	4
		χ_{200}		
1	0.76	0.63	0.16	0.03
2	0.64	-0.76	0.00	-0.14
3	0.26	0.16	-0.90	0.13
4	-0.10	0.30	-0.12	-0.90
		Outgoing Longwave Radiation		
1	0.98	-0.18	0.07	-0.02
2	-0.19	-0.97	-0.01	-0.11
3	0.11	-0.15	-0.73	0.56
4	0.07	0.17	-0.62	-0.68
		Q_{215}		
1	0.90	0.02	0.24	-0.24
2	-0.01	-0.93	0.23	0.16
3	0.17	-0.22	-0.40	-0.34
4	0.14	0.15	0.11	0.37
		T_{100}		
1	0.43	-0.57	0.01	-0.66
2	0.52	0.38	0.70	-0.06
3	-0.78	0.26	-0.08	-0.26
4	0.40	0.71	-0.13	0.04
		Q_{100}		
1	-0.83	-0.53	-0.02	0.09
2	0.53	-0.81	0.17	-0.02
3	0.33	0.02	-0.40	0.71
4	0.21	-0.33	-0.67	-0.40

EEOF, extended empirical orthogonal function.

6.2. Relationships Among Fields

From Figure 4, it is apparent that some of the fields have fairly coherent relationships with other fields. To quantify these relationships, we calculate the correlation between the leading EEOFs of each field with those of the other fields. Table 2 shows these correlations. Water vapor at 215 hPa is 180° out of phase with all the other fields, as indicated by the negative correlations in its rows and columns: In the convective phase of the TIO, velocity potential is low, OLR is low (high clouds), 215-hPa water vapor is high, 100-hPa temperature is low, and 100-hPa water vapor is low.

Velocity potential generally has the highest correlations with other fields, and 100-hPa temperature has the lowest. Velocity potential, which has been used in many dynamical studies of the TIO, is evidently the best indicator variable for these other upper tropospheric fields especially when considering the connection to 100 hPa.

The fact that water vapor at 215 and 100 hPa behaves oppositely in response to the TIO is consistent with Stratospheric Aerosol and Gas Experiment (SAGE) II climatology [*Rind et al.*, 1993], which showed that the mean distribution of upper tropospheric water vapor (300 and 150 hPa) had maxima in the tropical convective areas, while the 100-hPa distribution had a minimum in the same locations. (The SAGE II data are very sensitive to clouds, unlike MLS.) MLS data at 147 hPa confirm this antiphase relationship; spatially binning

the data as described above, the 147- and 215-hPa water vapor data have correlations of 0.83 for V422 (probably indicating that the V422 retrieval of 147-hPa data relies too heavily on values at 215 hPa), 0.62 for V490, and 0.54 for V5. Prominent eastward moving features in the 215-hPa data also appear in the 147-hPa data.

Consequently, it appears that both in the time mean and on intraseasonal timescales, there is a level somewhere between 147 and 100 hPa at which the water vapor response to convection changes sign. That is, convection moistens the upper troposphere up to that level and dries the upper troposphere and tropopause region above that level.

6.3. The 100-hPa Temperature and Water Vapor

It is surprising that the two fields that are least correlated (both the EEOFs and the original data) are the two fields at 100 hPa. Yet their EEOFs are each correlated with those of χ_{200}. This is partly because of the different behavior of the two fields in the Western Hemisphere, where water vapor behaves much like χ_{200}. As a consequence of this behavior in the Western Hemisphere, the TIO signature is more apparent in 100-hPa water vapor than in 100-hPa temperature.

There are several possible factors that may combine to explain the difference between the temperature and water vapor fields.

1. The two fields are related through different processes in the Eastern and Western Hemispheres. For example, convection in the Eastern Hemisphere may produce local saturation and drying, while free Kelvin waves in the Western Hemisphere may produce large-scale vertical motions.

2. The vertical gradients of the two fields are different.

3. The characteristics (e.g., vertical resolution) of the two data sets are different.

The first possibility seems plausible from looking at

Table 2. Correlations Between $EEOF_m$ of Different Fields

	Field				
	χ_{200}	OLR	Q_{215}	T_{100}	Q_{100}
EEOF 1					
χ_{200}	1.00	0.82	-0.76	0.47	0.71
OLR		1.00	-0.76	0.42	0.47
Q_{215}			1.00	-0.07	-0.57
T_{100}				1.00	0.28
Q_{100}					1.00
EEOF 2					
χ_{200}	1.00	0.81	-0.75	0.45	0.71
OLR		1.00	-0.76	0.38	0.46
Q_{215}			1.00	-0.06	-0.57
T_{100}				1.00	0.23
Q_{100}					1.00

Plate 3, which shows that temperature and water vapor tend to vary in the same sense between about 60° and 120°. Aircraft observations of tropical water vapor show saturation more commonly in convective regions than in the tropical eastern Pacific [*Kelly et al.*, 1993]. Consequently, the vertical gradients are different in the two regions too, which could provide part of the explanation for the difference.

The third possibility is also plausible. The two data sets have rather different characteristics; one is remotely sensed, and the other is generated by global reanalyses using a general circulation model. The issue of vertical resolution is particularly important. As noted in section 2, the 100-hPa water vapor measurement actually represents a layer probably some 4 km thick, mostly at altitudes above 100 hPa. By contrast, the reanalyses have finer vertical resolution and do almost as well as high-resolution radiosonde data at revealing TIO variations in temperature near the tropopause (G. Kiladis, personal communication, 1999, 2000). There is ample evidence that the TIO is both sharply attenuated and of small vertical scale in the lower stratosphere. *Mote et al.* [1998] stated that the spectral power of water vapor variations in the 30- to 70- day band drops by an order of magnitude between 100 and 68 hPa, the next higher MLS level. Analysis of radiosonde temperatures by G. Kiladis (personal communication, 1999) reveals that the vertical scale of the TIO is so shallow in the lower stratosphere that the phase undergoes a complete reversal between 100 and 70 hPa, in agreement with the earlier study of *Hendon and Liebmann* [1990]. For disturbances that are sharply attenuated above the tropopause and for disturbances with shallow vertical structure in the vicinity of 100 hPa, the variations in temperature could be well represented by ERA data but the variations in water vapor could be strongly diminished in the MLS retrieval. Taken together, the attenuation and small vertical scale of the TIO combined with the poor vertical resolution of MLS in the lower stratosphere imply that the true variation in water vapor at 100 hPa associated with the TIO could be substantially stronger than indicated by the MLS instrument. As for the behavior of 100-hPa temperature, it is possible that the discrepancy in the Western Hemisphere is related to the paucity of observations that could constrain the ECMWF analysis.

7. Discussion and Conclusions

We have shown that the well-known tropical intraseasonal oscillation has a fairly robust and important signature on upper tropospheric water vapor at 215 hPa (and, not shown, at 147 hPa) and that the TIO signature in OLR is very coherent with the signature in water vapor. Convection associated with the TIO moistens the upper troposphere, an effect that operates only where a strong signature of the TIO in convection is found: between about 60°E and 210°E. By contrast, the dynamical fields (velocity potential at 200 hPa and

temperature at 100 hPa), although coherent with OLR and Q_{215} in the Eastern Hemisphere, have very different behavior east of 210°E. Variations in velocity potential show the familiar increase in phase speed, while the temperature at 100 hPa shows an odd reduction in horizontal phase speed, which may in fact be related to a change in the vertical phase speed.

Water vapor at 100 hPa clearly responds to the TIO as well, though the variations are rather subtle and at first glance unrelated to the variations in temperature at the same level. Its similarity to velocity potential in the Western Hemisphere suggests that there, at least, the origin of the anomalies is purely dynamical and not induced by radiative anomalies above cold cloud tops. One possible explanation for the difference between the water vapor and temperature fields is simply that the water vapor data are more smeared out in the vertical and that the vertical wavelength of the TIO signal near the tropopause is substantially different in the Western Hemisphere than in the Eastern Hemisphere.

Our analysis demonstrates, for the first time on a global scale, that the response of 100-hPa water vapor to the TIO is out of phase with the water vapor response at 215 and 147 hPa. While the convectively active phase moistens the upper troposphere, the tropopause region becomes dryer. The tendency of the tropopause to become higher, colder, and dryer during active convection is well known from observational campaigns using radiosondes equipped with frost-point hygrometers [*Vömel et al.*, 1995]. Unclear from such local observations, however, is the horizontal extent of the water vapor response in relation to convection. Tropical convection is organized within cloud clusters and superclusters [*Hendon and Liebmann*, 1994; *Dunkerton and Crum*, 1995], but circulation anomalies associated with the intraseasonal oscillation are much broader in longitudinal extent. Our water vapor results at 100 hPa, although consistent with ground-based observations of tropopause behavior, do not adequately resolve the horizontal structure of mesoscale cloud clusters; therefore we cannot see the local response to tropical convection. Instead, these results suggest that water vapor anomalies visible from satellite extend over a wide range of longitudes, including regions where the TIO is decoupled from convection (i.e., in the Western Hemisphere).

Interpretation of the 100-hPa water vapor data is complicated by uncertainty as to which levels are actually responsible for this signal and to what extent the data at this level are spuriously affected by water vapor from a slightly higher level (68 hPa). Until this uncertainty is resolved, and a connection to nearby temperature anomalies is made, we cannot be certain of the cause of the 100-hPa water vapor signal, whether it involves upward displacement of the water vapor gradient, horizontal transport, change of saturation mixing ratio, or some combination of these effects.

Clearly, the tropopause region is affected by the TIO, both directly by convection and indirectly by the slow, shallow Kelvin waves that it generates in the lower

stratosphere. More work is needed to understand how these phenomena interact and how they vary zonally, especially in the eastern Pacific. It would be useful to check these results against station data, but in the eastern Pacific there are hardly any stations. Satellite measurements of water vapor there are plentiful, but instruments with better vertical resolution than MLS in the vicinity of the tropopause (e.g., the Halogen Occultation Experiment, also aboard UARS) do not have adequate temporal coverage to study the TIO.

Two new instruments currently scheduled for launch on the EOS CHEM satellite in 2002 may shed light on these questions. The High-Resolution Dynamics Limb Sounder (HIRDLS) is an infrared instrument that will achieve 1-km vertical resolution and is intended to be suitable for studying the lower stratosphere and tropopause region. "Observations of the lower stratosphere are improved through the use of special narrow and more transparent spectral channels" (from http://www.eos.ucar.edu/hirdls/home.html). The EOS MLS [*Waters et al.*, 1999] is an improved version of the MLS instrument discussed here, and has improved bandwidth, which should improve the accuracy in the lower stratosphere and upper troposphere. Its closely spaced scan pattern should give improved vertical resolution of 1.5–2 km. Both HIRDLS and EOS MLS will have more frequent scans, giving better horizontal resolution as well. Together, these instruments will reveal in better detail the TIO response of water vapor in the important layer between 200 and 100 hPa.

References

Barath, F., et al., The Upper Atmosphere Research Satellite Microwave Limb Sounder instrument, *J. Geophys. Res., 98*, 10,751–10,762, 1993.

Brown, R.G., and C. Zhang, Variability of midtropospheric moisture and its effect on cloud-top height distribution during TOGA COARE, *J. Atmos. Sci., 54*, 2760–2774, 1997.

Chen, B., and M. Yanai, Comparison of the Madden-Julian oscillation (MJO) during the TOGA COARE IOP with a 15-year climatology, *J. Geophys. Res., 105*, 2139–2149, 2000.

Clark, H.L., R.S. Harwood, P.W. Mote, and W.G. Read, Variability of water vapor in the tropical upper troposphere as measured by the Microwave Limb Sounder on UARS, *J. Geophys. Res., 103*, 31,695–31,707, 1998.

Dunkerton, T.J., and M.P. Baldwin, Observation of 3–6 day meridional wind oscillations over the tropical Pacific, 1973–1992: Horizontal structure and propagation, *J. Atmos. Sci., 52*, 1585–1601, 1995.

Dunkerton, T.J., and F.X. Crum, Eastward propagating ∼2- to 15-day equatorial convection and its relation to the tropical intraseasonal oscillation, *J. Geophys. Res., 100*, 25,781–25,790, 1995.

Elson, L.S., W.G. Read, J.W. Waters, P.W. Mote, J.S. Kinnersley, and R.S. Harwood, Space-time variations in water vapor as observed by the UARS Microwave Limb Sounder, *J. Geophys. Res., 101*, 9001–9015, 1996.

Gibson, J.K., P. Kallberg, S. Uppala, A. Hernandez, A. Nomura, and E. Serrano, ERA description, *Re-analysis Project Rep. Ser. 1*, Eur. Cent. for Medium-Range Weather Forecasts, Reading, England, 1997.

Hendon, H.H., and J. Glick, Intraseasonal air-sea interaction in the tropical Indian and Pacific oceans, *J. Clim., 10*, 647–661, 1997.

Hendon, H.H., and B. Liebmann, The intraseasonal (30–50 day) oscillation of the Australian summer monsoon, *J. Atmos. Sci., 47*, 2909–2923, 1990.

Hendon, H.H., and B. Liebmann, Organization of convection within the Madden-Julian oscillation, *J. Geophys. Res., 99*, 8073–8083, 1994.

Hendon, H.H., and M.L. Salby, The life-cycle of the Madden-Julian oscillation, *J. Atmos. Sci., 51*, 2225–2237, 1994.

Kelly, K.K., M.H. Proffitt, K.R. Chan, M. Loewenstein, J.R. Podolske, S.E. Strahan, J.C. Wilson, and D. Kley, Water vapor and cloud water measurements over Darwin during the STEP 1987 tropical mission, *J. Geophys. Res., 98*, 8713–8723, 1993.

Kiladis, G.N., and K.M. Weickmann, Circulation anomalies associated with tropical convection during northern winter, *Mon. Weather Rev., 120*, 1900–1923, 1992.

Knutson, T.R., and K.M. Weickmann, 30–60 day atmospheric oscillations: Composite life cycles of convection and circulation anomalies, *Mon. Weather Rev., 115*, 1407–1437, 1987.

Liebmann, B., and C.A. Smith, Description of a complete (interpolated) outgoing longwave radiation dataset, *Bull. Am. Meteorol. Soc., 77*, 1275–1277, 1996.

Madden, R.A., and P.R. Julian, Detection of a 40–50 day oscillation in the zonal wind in the tropical Pacific, *J. Atmos. Sci., 28*, 702–708, 1971.

Madden, R.A., and P.R. Julian, Observations of the 40–50 day tropical oscillation—A review, *Mon. Weather Rev., 122*, 814–837, 1994.

Matthews, A.J., and G.N. Kiladis, The tropical-extratropical interaction between high frequency transients and the Madden-Julian oscillation, *Mon. Weather Rev., 127*, 661–677, 1999.

Matthews, A.J., B.J. Hoskins, J.M. Slingo, and M. Blackburn, Development of convection along the SPCZ within a Madden-Julian oscillation, *Q. J. R. Meteorol. Soc., 122*, 669–688, 1996.

McPhaden, M.J., Genesis and evolution of the 1997–98 El Niño, *Science, 283*, 950–954, 1999.

Mote, P.W., K.H. Rosenlof, M.E. McIntyre, E.S. Carr, J.C. Gille, J.R. Holton, J.S. Kinnersley, H.C. Pumphrey, J.M. Russell III, and J.W. Waters, An atmospheric tape recorder: The imprint of tropical tropopause temperatures on stratospheric water vapor, *J. Geophys. Res., 101*, 3989–4006, 1996.

Mote, P.W., T.J. Dunkerton, and H.C. Pumphrey, Subseasonal variations in lower stratospheric water vapor, *Geophys. Res. Lett., 25*, 2445–2448, 1998.

Pumphrey, H.C., Validation of a new prototype water vapor retrieval for the UARS Microwave Limb Sounder, *J. Geophys. Res., 104*, 9399–9412, 1999.

Read, W.G., J.W. Waters, D.A. Flower, L. Froidevaux, R.F. Jarnot, D.L. Hartmann, R.S. Harwood, and R.B. Rood, Upper tropospheric water vapor from UARS MLS, *Bull. Am. Meteorol. Soc., 76*, 2381–2389, 1995.

Reber, C.A., The Upper Atmosphere Research Satellite (UARS), *Geophys. Res. Lett., 20*, 1215–1218, 1993.

Rind, D., E.-W. Chiou, W. Chu, S. Oltmans, J. Lerner, J. Larsen, M.P. McCormick, and L. McMaster, Overview of the Stratospheric Aerosol and Gas Experiment II water vapor observations: Method, validation, and data characteristics, *J. Geophys. Res.*, *98*, 4835–4856, 1993.

Vömel, H., S.J. Oltmans, D. Kley, and P.J. Crutzen, New evidence for the stratospheric dehydration mechanism in the equatorial Pacific, *Geophys. Res. Lett.*, *22*, 3235–3238, 1995.

Waters, J.W., Microwave Limb Sounding, in *Atmospheric Remote Sensing by Microwave Radiometry*, edited by M.A. Janssen, pp. 383–496, John Wiley, New York, 1993.

Waters, J.W., et al., The UARS and EOS Microwave Limb Sounder (MLS) experiments, *J. Atmos. Sci.*, *56*, 194–218, 1999.

Weare, B.C., and J.S. Nasstrom, Examples of extended empirical orthogonal function analysis, *Mon. Weather Rev.*, *110*, 481–485, 1982.

Wheeler, M., and G.N. Kiladis, Convectively coupled equatorial waves: Analysis of clouds and temperature in the wavenumber-frequency domain, *J. Atmos. Sci.*, *56*, 374–399, 1999.

H. L. Clark, R. S. Harwood, and H. C. Pumphrey, Department of Meteorology, University of Edinburgh, Edinburgh EH9 3JZ, Scotland, UK. (H.Clark@ed.ac.uk; r.harwood@ed.ac.uk; hcp@met.ed.ac.uk)

T. J. Dunkerton and P. W. Mote, Northwest Research Associates, PO Box 3027, Bellevue, WA 98009. (mote@nwra.com, tim@nwra.com)